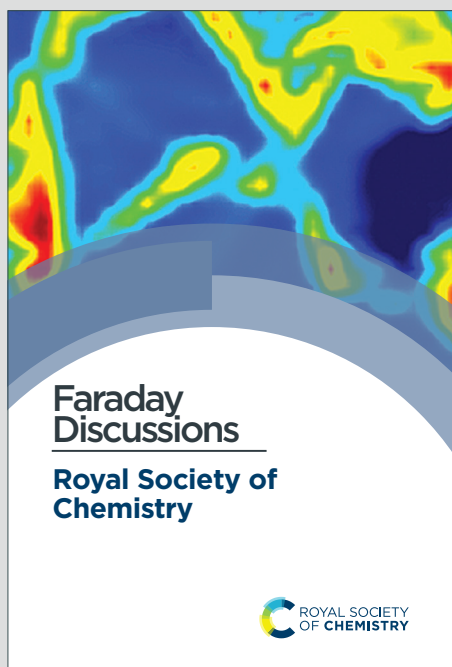


# Faraday Discussions

Accepted Manuscript



This is an Accepted Manuscript, which has been through the Royal Society of Chemistry peer review process and has been accepted for publication.

Accepted Manuscripts are published online shortly after acceptance, before technical editing, formatting and proof reading. Using this free service, authors can make their results available to the community, in citable form, before we publish the edited article. We will replace this Accepted Manuscript with the edited and formatted Advance Article as soon as it is available.

You can find more information about Accepted Manuscripts in the [Information for Authors](#).

Please note that technical editing may introduce minor changes to the text and/or graphics, which may alter content. The journal's standard [Terms & Conditions](#) and the [Ethical guidelines](#) still apply. In no event shall the Royal Society of Chemistry be held responsible for any errors or omissions in this Accepted Manuscript or any consequences arising from the use of any information it contains.

This article can be cited before page numbers have been issued, to do this please use: S. Drvaric Talian, J. Moskon, B. Slabajna, . Saksida, O. Luzanin, T. Šlosar, E. Tchernychova, I. Dacrema, N. Latas, U. Košir, G. Kapun, M. Gaberscek and R. Dominko, *Faraday Discuss.*, 2026, DOI: 10.1039/D6FD00029K.



1 with the electrolyte and which controls the electrode's performance. Unlike the well-  
2 understood Solid Electrolyte Interphase (SEI) on lithium metal—which is ionically  
3 conductive yet electronically insulating—the nature and function of the film on Mg metal  
4 anodes remain a subject of debate.

5 Currently, the research often operates under the assumption that the interphase  
6 formed on Mg metal is similar to a Li SEI. As a result, studies commonly aim to improve  
7 Mg metal performance through controlling the morphology and chemical composition  
8 of its passive layer, in effect aiming to facilitate  $Mg^{2+}$  migration. The approach often  
9 involves changes in electrolyte formulation, which affects the  $Mg^{2+}$  solvation structure  
10 and directly controls the composition of the passive layer.<sup>1,2</sup> Another possibility is  
11 interface engineering, which employs additives<sup>3,4</sup> or formation of optimized artificial  
12 passivation layers<sup>5-7</sup>.

13 Nevertheless, fundamental question on whether or not the Mg passivation layer  
14 actually permits ionic transport, or does it need to physically rupture to expose the  
15 active metal<sup>8,9</sup>, remains. Determining whether the interphase behaves as a true SEI or  
16 a blocking passivation film is critical, since it governs the faradaic processes,  
17 impedance losses, and overall reversibility of the anode. In this paper, we characterize  
18 the Mg metal interphase in a representative chloride-based glyme electrolyte. Although  
19 this group of electrolytes is corrosive toward current collectors and other battery  
20 components, they are compatible with electrophilic electrodes due to their non-  
21 nucleophilic nature and are commercially available, making them an good model  
22 system for studying fundamental interfacial mechanisms

23 We employed electrochemical impedance spectroscopy and coupled it with advanced  
24 morphological and chemical analyses (FIB-SEM, TEM/STEM, and XPS). By proposing  
25 a dual-layer model, we explain the apparent discrepancy between electrochemical  
26 data, which suggests a thin barrier, and morphological observations of thick porous  
27 layers. Furthermore we show that the Mg interphase exhibits significant electronic  
28 conductivity while remaining ionically resistive through polysulfide experiments and  
29 identical-location microscopy. This "anti-SEI" behavior explains the observed  
30 asymmetry between stripping and plating processes and necessitates a paradigm shift  
31 in how Mg metal interfaces are modeled and engineered.

32

33

## 34 **Experimental details**

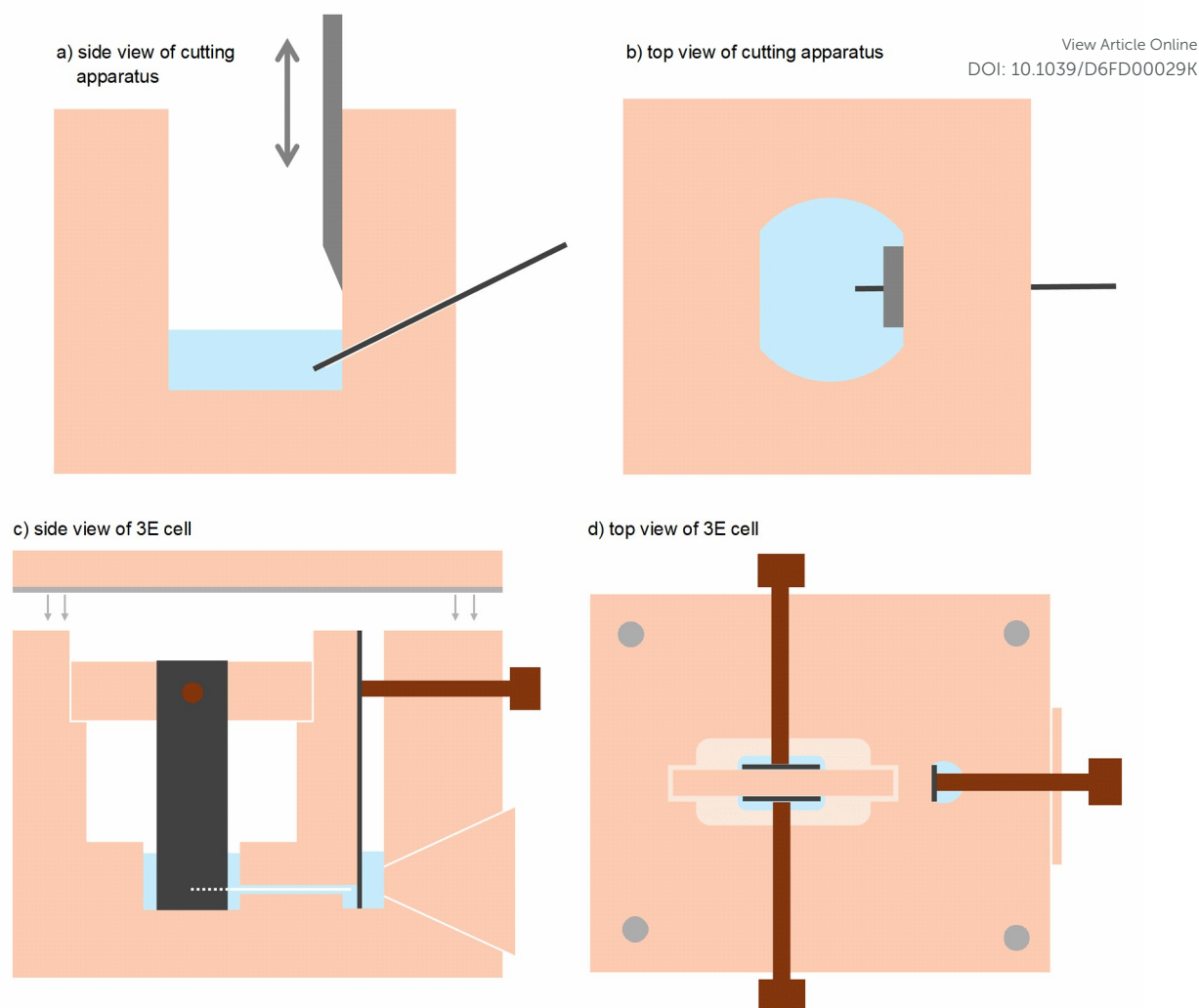
35 All electrochemical cell components were handled in an argon filled glovebox  
36 (Mbraun), where oxygen and water content was kept below 1 ppm. Mg (100  $\mu$ m thick  
37 foil, Changsha Rich Nonferrous metals, 99.95%) was brushed with sanding paper in  
38 eight different directions with P1200 sanding paper before electrodes were cut from it.  
39 Electrodes intended for cells with leaner electrolyte conditions (pouch cell casing,  
40 Swagelok casing) were then punched out using a round puncher. Electrodes for larger



1 electrolyte quantity cell experiment were cut with scissors into 1x4 cm rectangles for  
2 working electrode (WE) and counter electrode (CE) and 0.5 x 5 cm rectangle for  
3 reference electrode (RE). Electrodes for the experiment with added  $\text{Li}_2\text{S}_8$  electrolyte  
4 were round punched and pre-passivated by soaking them in a vial with the Mg-based  
5 electrolyte for 1 h before washing them with 1,3-dioxolane solvent. Li metal (Gelon,  
6 200  $\mu\text{m}$  ribbon) was used without pretreatment by punching out disc electrodes with a  
7 round puncher. Glassy carbon discs (GC, 2  $\text{cm}^2$ , HTW) were dried at 50  $^\circ\text{C}$  overnight,  
8 placed in the glovebox and used as electrodes without pretreatment.

9 Mg electrodes intended for chemical and morphological investigation of passive layer  
10 growth were cut from 1.6 mm diameter Mg rods (Goodfellow, 99.9%) while soaking in  
11 the Mg-based electrolyte, using a cutting apparatus manufactured in-house (**Figs. 1a**  
12 **and b**). The apparatus consisted of a PEEK plastic cup with an internal diameter of  
13 approximately 2 cm and a height of 5 cm, designed to hold the electrolyte (2 mL was  
14 used). The top- down view of the cup opening was shaped like a truncated circle. A 2  
15 mm diameter hole was drilled at a 30 $^\circ$  inclination (from horizontal) into the cup wall on  
16 the truncated side, with the opening positioned 5 mm above the inside bottom edge of  
17 the cup. This allowed placement of a Mg rod into the electrolyte compartment (black  
18 line in the scheme) without electrolyte spillage. The cup was fixed to a manual disc  
19 puncher (MTI Corporation), which was placed inside the glovebox and modified by  
20 replacing the puncher with a guillotine-like blade capable of cutting the Mg rod inside  
21 the electrolyte compartment. To ensure a cleaner cut, the blade was plunged into the  
22 apparatus alongside the inside truncated edge of the cup.





View Article Online  
DOI: 10.1039/D6FD00029K

1  
2 **Figure 1:** schematics of the Mg rod cutting apparatus in a) side view and b) top view.  
3 Schematics of the 3E cell in a) side view and b) top view.

4 The Mg-based electrolyte in all experiments was 0.4 M  $\text{MgCl}_2$ , 0.4 M magnesium  
5 bis(trifluoromethanesulfonyl)imide ( $\text{MgTFSI}_2$ ) in tetraglyme (TEGDME) : 1,3-dioxolane  
6 (DOL) 1:1 (v:v) solvent mixture. All components were dried before use:  $\text{MgTFSI}_2$   
7 (Solvionic, 99.5) was dried overnight under vacuum at 220 °C,  $\text{MgCl}_2$  (Thermo Fisher  
8 Scientific, 99.99) was used as received, TEGDME (99%, Acros) and DOL (Sigma-  
9 Aldrich, HPLC grade, 99.9%) solvents were dried using 4 Å molecular sieves for five  
10 days, refluxed overnight with a Na/K alloy, and subsequently purified by fractional  
11 distillation. All procedures were done inside the glovebox to prevent contamination with  
12 water. The final water content was determined by Karl Fischer titration (Mettler Toledo,  
13 C20) and confirmed to be below 1 ppm. The electrolyte was prepared in the glovebox  
14 in a volumetric flask by first dissolving  $\text{MgTFSI}_2$  in the solvent mixture. Then  $\text{MgCl}_2$  was  
15 added and dissolved, until finally the solvent mixture was added to the volumetric  
16 marking on the flask.

17  $\text{Li}_2\text{S}_8$  powder used for preparation of the polysulfide solution was synthesized by mixing  
18 stoichiometric amounts of Li and sulfur (Sigma Aldrich, 99.98%) in tetrahydrofuran



1 (Sigma Aldrich, 99.9%), heating the mixture to 50 °C until the reactants dissolved, and  
2 isolating the product under reduced pressure inside the glovebox. 100 mM  $\text{Li}_2\text{S}_8$   
3 solution in TEGDME:DOL 1:1 (v:v) mixture was prepared analogously to the Mg  
4 electrolyte in a volumetric flask inside the glovebox. Since polysulfides tend to  
5 disproportionate, the concentration of this catholyte solution should be considered  
6 nominal. For the *operando* polysulfide addition experiment, 0.5 M polysulfide solution  
7 was prepared in the same solvent mixture.

8 Symmetrical lean-electrolyte Mg||Mg cells were assembled by placing a 13 mm in  
9 diameter glass fiber (GF-A, Whatman, 260  $\mu\text{m}$ ) separator between the two brushed  
10 Mg electrodes 12 mm in diameter and wetting it with 80  $\mu\text{L}$  of the Mg electrolyte. The  
11 stack was sealed inside a Swagelok type cell with graphite discs (Ted Pella, Carbon  
12 Planchets 10 mm) between Swagelok cell stainless steel current collector rods and the  
13 Mg electrodes in order to minimize corrosion of the casing by the chloride containing  
14 electrolyte. Symmetrical Li||Li cells were assembled by placing a 18 mm in diameter  
15 Celgard 2320 separator between two Li electrodes 16 mm in diameter and wetting it  
16 with 20  $\mu\text{L}$  of 1 M  $\text{LiPF}_6$  in ethylene carbonate (EC): diethyl carbonate (DEC) 1:1 (v:v)  
17 electrolyte (LP40, Elyte). The stack was placed inside a pre-fabricated and dried triplex  
18 (PE 90  $\mu\text{m}$ /Al 10  $\mu\text{m}$ /PET 20  $\mu\text{m}$ ) pouch casing with Ni current collectors and heat  
19 sealed inside the glovebox. Stack pressure was ensured by an external clip placed on  
20 the pouch cell, which maintained approximately 150 kPa of pressure. Cells with  
21 polysulfide based electrolyte were assembled with the use of pre-soaked Mg  
22 electrodes or GC electrodes and glass fiber separators with the same procedure as Li  
23 metal electrodes – by placing them in triplex pouch casing and heat sealing it.

24 For the flooded three-electrode cell configuration, an in-house cell from polypropylene  
25 (PP) plastic was used (**Figs. 1c and d**). The cell contains two compartments, one for  
26 WE and CE (left in scheme) and one for RE (right in scheme) connected via an  
27 electrolyte bridge in the form of a glass fiber protruding into both compartments near  
28 the inside bottom edges of the compartments (white line in **Fig. 1c**). The WE and CE  
29 are placed parallel to each other and parallel to the fiber placed in their middle in a 4 x  
30 15 mm electrolyte compartment. The WE and CE electrode strips are kept 4 mm apart  
31 by a PP separator block placed above the electrolyte compartment. The WE and CE  
32 are fixed to the separator block with flat end screws from the sides of the cell, which  
33 also serve as current collectors. The WE/CE compartment holds 0.7 mL of the  
34 electrolyte. The RE compartment is narrower (5 mm diameter). The RE is contacted  
35 by a flat end screw fixing the Mg strip into the body of the cell perpendicular to the WE  
36 and CE contact screws. The glass fiber bridge can be extracted for cleaning or  
37 replacement by unscrewing a cap from the bottom side next to the RE compartment.  
38 The cell can be sealed from the top with a lid, a gasket and four screws and taken  
39 outside the glovebox for short measurements, but we have not tested its sealing  
40 durability against longer periods of atmosphere exposure.

41 Impedance spectra of the examined symmetrical cells were measured at OCV with a  
42 VMP-3e Bio-logic potentiostat/galvanostat. 5 mV (rms) amplitude and 1 MHz-20 mHz



1 frequency range were employed, except in the operando experiment, where we limited  
2 the frequency range to 1 MHz-100 mHz. Impedance spectra were processed in  
3 Zview®, version 4 by fitting the higher frequency region of the visible arc (region with  
4 less distortions) with an arbitrary  $R_{el}-R(CPE)$  circuit in order to extract the changes in  
5 the arc resistance ( $R$ ) and capacitance ( $C$ ) values. The latter were calculated from the  
6 obtained  $CPE-P$  (here denoted as  $P$ ) and  $CPE-T$  (denoted as  $T$ ) parameters using Eq.  
7 1.

$$C = R \frac{1-P}{P} \frac{1}{T^P} \quad \text{Eq. 1}$$

8  
9 Before chemical or morphological analysis of the Mg electrode samples, the electrodes  
10 were washed with DOL and dried before using vacuum-transfer holders to transfer  
11 them from the glovebox to the intended instrument.

12 Surface morphology of the electrodes cycled at different currents was examined using  
13 SUPRA 35VP (Zeiss, Germany) scanning electron microscope. The acceleration  
14 voltage for SEM imaging was set to 1.0 kV. For identical location scanning electron  
15 microscopy HR-SEM Apreo 2S (Thermo Fisher Scientific) was employed. Micrographs  
16 were measured at an accelerating voltage of 2.0 kV and a beam current of 25 pA via  
17 an Everhart-Thornley detector (ETD). To maintain inert conditions, all samples were  
18 transferred from the Ar-filled glovebox to the microscope vacuum chamber (and back)  
19 using a CleanConnect Sample Transfer System. The Mg foil substrate was initially  
20 rinsed with DOL inside an Ar-filled glovebox to remove bulk electrolyte. After  
21 transferring to the SEM, micrographs of different deposits were recorded to enable  
22 direct comparison with the same locations after the deposits were subsequently  
23 removed. The sample was returned to the Ar-filled glovebox for localized deposit  
24 removal. Selected Mg deposits were mechanically delaminated from the substrate  
25 using a polyethylene (PE) wedge as a scraping tool. The sample was then re-  
26 transferred to the SEM to characterize the morphology and elemental composition of  
27 the newly exposed sites. A washing procedure was performed to remove the  
28 electrolyte salt residues that were found after the deposits were removed. A glass  
29 pipette was used to apply a single drop of DOL directly onto the regions of interest on  
30 the sample still remaining on the SEM holder. The solvent was allowed to evaporate  
31 (30 seconds), and this micro-washing cycle was repeated five times per site. Final HR-  
32 SEM imaging was then performed.

33 FIB cross-sectional analysis was performed by using a FIB-SEM Helios G5 UC  
34 equipped with a multi gas injection system (GIS), an CleanConnect sample transfer  
35 system (Thermo Fisher Scientific, The Netherlands) and Ultim max 65 EDX detector  
36 (Oxford, UK). Samples and the FIB lift-out grid were mounted into a CleanConnect  
37 capsule inside an Ar-filled glovebox and transferred in Ar 5.0 overpressure (200 mbar)  
38 directly to the FIB instrument. The sample surface was initially protected by a 500 nm  
39 Pt layer using electron beam induced deposition (EBID, 2 kV at 0.4 nA). Subsequently,  
40 an additional Pt layer was deposited using Ga<sup>+</sup> ion beam induced deposition (IBID, 30



1 kV at 0.23 nA) to achieve a protective layer with a final thickness of 1.8  $\mu\text{m}$ .  
2 Morphological images of the cross sections were recorded using a low energy electron  
3 beam (1 kV @ 50 pA) by using standard ETD and ICE detectors. Detailed information  
4 at the SEI region was acquired using InColumn integrated TLD detector and a pre-  
5 monochromated electron beam at 500 V energy and 6.3 pA beam current.

6 TEM lamella was prepared by first thinning the sample to 250 nm thickness using FIB  
7 at 30 kV by sequentially reducing ion beam currents from 780 pA to 80 pA due to  
8 sample sensitivity. Subsequently, the lamella was carefully thinned to 100 nm using  
9 FIB at 16 kV with a 24 pA beam current. Afterwards, the lamella was sequentially  
10 polished on both sides using FIB at 5 kV at 44 pA, 2 kV at 25 pA, and 1 kV at 20 pA  
11 until electron transparency ( $\sim 80$  nm) was achieved. The prepared lamella sample was  
12 transferred with a vacuum transfer system directly from the FIB chamber to the  
13 glovebox, where it was mounted to the TEM vacuum transfer holder.

14 X-ray photoelectron spectroscopy (XPS) measurements were carried out using a  
15 Versaprobe 3 AD (Phi, Chanhassen, USA) system equipped with a monochromatic Al-  
16 K $\alpha$ 1 excitation source (1486.7 eV). Spectra were collected using a 200  $\mu\text{m}$  spot size  
17 with the charge neutralizer enabled, as the Mg rods were mounted on non-conductive  
18 double-sided Scotch tape. High-resolution spectra were recorded at a pass energy of  
19 27 eV and a step size of 0.05 eV. Depth profiling was conducted by sputtering a 1 x 1  
20 mm<sup>2</sup> area using 2 kV Ar<sup>+</sup> ions at a chamber pressure of approximately  $2 \times 10^{-7}$  Pa for  
21 a total duration of 80 minutes, in intervals of 3 x 0.1, 0.2, 0.5, 3 x 1, 2 x 2, 3 x 4, and  
22 12 x 5 seconds. The energy scale was corrected by setting the C 1s peak of  
23 adventitious carbon to 284.8 eV. Data analysis was done using MultiPak.

24 The samples prepared for scanning transmission electrom microscopy (STEM) using  
25 FIB were transferred from the glovebox to the microscope using a vacuum-transfer  
26 TEM holder (Gatan, USA). STEM analyses were carried out on a probe Cs-corrected  
27 JEOL ARM-200CF operated at an accelerating voltage of 80 kV to minimize beam  
28 damage. During these analyses, high-angle annular dark-field (HAADF) and annular  
29 bright-field (ABF) detectors were used simultaneously with collection semi-angles of  
30 95-370 mrad and 10-24 mrad, respectively.

## 31 Results

32 When the impedance of a magnesium metal electrode is characterized at open-circuit  
33 voltage (OCV), the spectra typically display a slightly deformed arc that increases in  
34 resistance, while its peak frequency decreases. If the time evolution of the data is  
35 plotted, the resistance increases almost linearly, the capacitance remains nearly  
36 constant, and the peak frequency decreases inversely with time (**Figs. 2a and 2b**). To  
37 begin understanding this impedance response, it is instructive to compare it to a more  
38 well-known metallic anode: lithium metal. The impedance response of a lithium metal  
39 electrode is usually explained by attributing the large high-frequency arc at  
40 intermediate frequencies to the resistance from Li<sup>+</sup> ion migration through the compact  
41 solid electrolyte interphase (SEI) layer on the electrode. There are additional, smaller

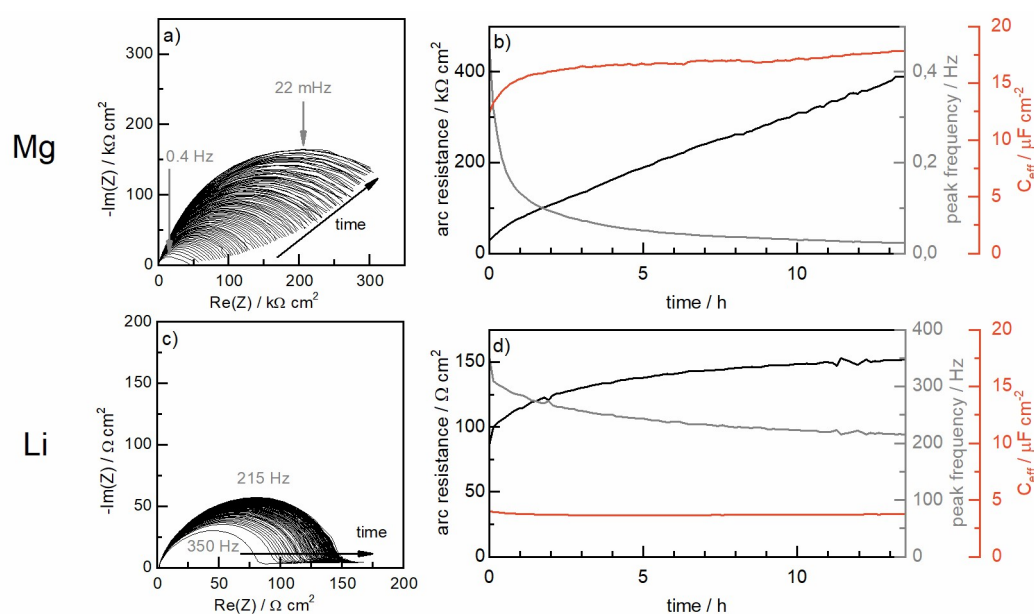


1 contributions at lower frequencies, corresponding to diffusion in the porous SEI and  
 2 porous separator layers<sup>10</sup> (**Fig. 2c**).

View Article Online  
 DOI: 10.1039/D6FD00029K

3 Let us now compare the response of Li and Mg electrodes. Both show the same  
 4 direction of changes for resistance and peak frequency, except that in the Li metal  
 5 electrode case, the arc resistance growth levels out (**Fig. 2d**). In the measured time  
 6 frame, the resistance of the high frequency arc in the Li metal EIS spectrum increases  
 7  $\times 2$ , while in the Mg case, the resistance increases  $\times 10$ . Importantly, the absolute value  
 8 of the resistance is about  $1000\times$  lower in the Li metal case – 75 to 150  $\Omega\cdot\text{cm}^2$  in Li vs.  
 9 40 to 400  $\text{k}\Omega\cdot\text{cm}^2$  in Mg. If the experiment with Mg is continued, the resistance  
 10 increases to over 1  $\text{M}\Omega\cdot\text{cm}^2$  in 72 h.

11



12

13 **Figure 2:** EIS spectra of a) Mg metal symmetrical cell at OCV and b) changes to the  
 14 resistance, capacitance and peak frequency over the first 13 hours of the experiment.  
 15 c) EIS spectra of Li metal symmetrical cell at OCV and d) changes to the resistance,  
 16 capacitance and peak frequency over the first 13 hours of the experiment.

17

18 Since the charge transfer reaction is considered negligible on Li metal, the drift in the  
 19 resistance of the high-frequency arc for Li electrodes is usually attributed to changes  
 20 in the transport properties of the SEI; that is, the SEI gradually becomes more ordered,  
 21 denser, or less defective, which decreases its specific ionic conductivity for  $\text{Li}^+$  ions<sup>11</sup>.  
 22 Importantly, the resistance growth cannot be associated with changes in SEI thickness,  
 23 since the capacitance remains constant with an approximate value of 4  $\mu\text{F}\cdot\text{cm}^2$ . As  
 24 this capacitance is directly correlated with the dielectric properties of the region  
 25 occupied by SEI, its constant value indicates very strongly that the volume (and thus  
 26 thickness) of this region remains constant over time.



1 When trying to understand the measured EIS changes in Mg metal anodes, one must  
2 first consider that unlike in lithium, the charge transfer reaction for this system is not  
3 negligible<sup>12</sup>. The response is therefore always a combination of the passive film  
4 resistance and the charge transfer reaction resistance, with the possibility that one is  
5 significantly larger and dominates the other.

6 Since the capacitance value remains similar ( $17 \mu\text{F}\cdot\text{cm}^2$ ), we assume, as in the case  
7 of lithium, that there are no significant geometrical changes associated with the  
8 phenomena observed in the spectra; that is, neither the thickness of the probed  
9 passive layer nor the surface area associated with double layer formation at the  
10 electrode changes. One possibility is that the measured response is dominated by the  
11 charge transfer reaction resistance, which increases due to a decreasing number of  
12 available reaction sites as a consequence of passive film evolution. Alternatively, the  
13 passive film resistance and charge transfer reaction resistance may be of similar  
14 importance, with the impedance spectra drift originating from both phenomena. Third,  
15 if we mirror the Li case, one possibility for the observed drift is that the charge transfer  
16 reaction resistance is significantly smaller than the passive layer resistance, and the  
17 resistance growth is due to the passive film reordering and becoming less conductive  
18 as the number of defects decreases.

19 If we assume that the measured capacitance originates from the passive film  
20 properties, we can estimate its thickness. Assuming a dielectric constant of 10 for the  
21 surface film, this would suggest a 0.5 nm thick passive layer in the magnesium case  
22 and 2 nm thick in the Li case. To determine the actual thickness of the passive film on  
23 Mg metal as well as its chemical composition and morphology, we conducted  
24 passivation experiments on Mg electrodes, which were cut inside the electrolyte and  
25 left to passivate for 1 h vs. for 72 h. In this extended time frame, the resistance  
26 increased for a factor of 25, while the capacitance of the passive layer increased by a  
27 factor of 2.4 ( $15$  to  $36 \mu\text{F}\cdot\text{cm}^2$ ).



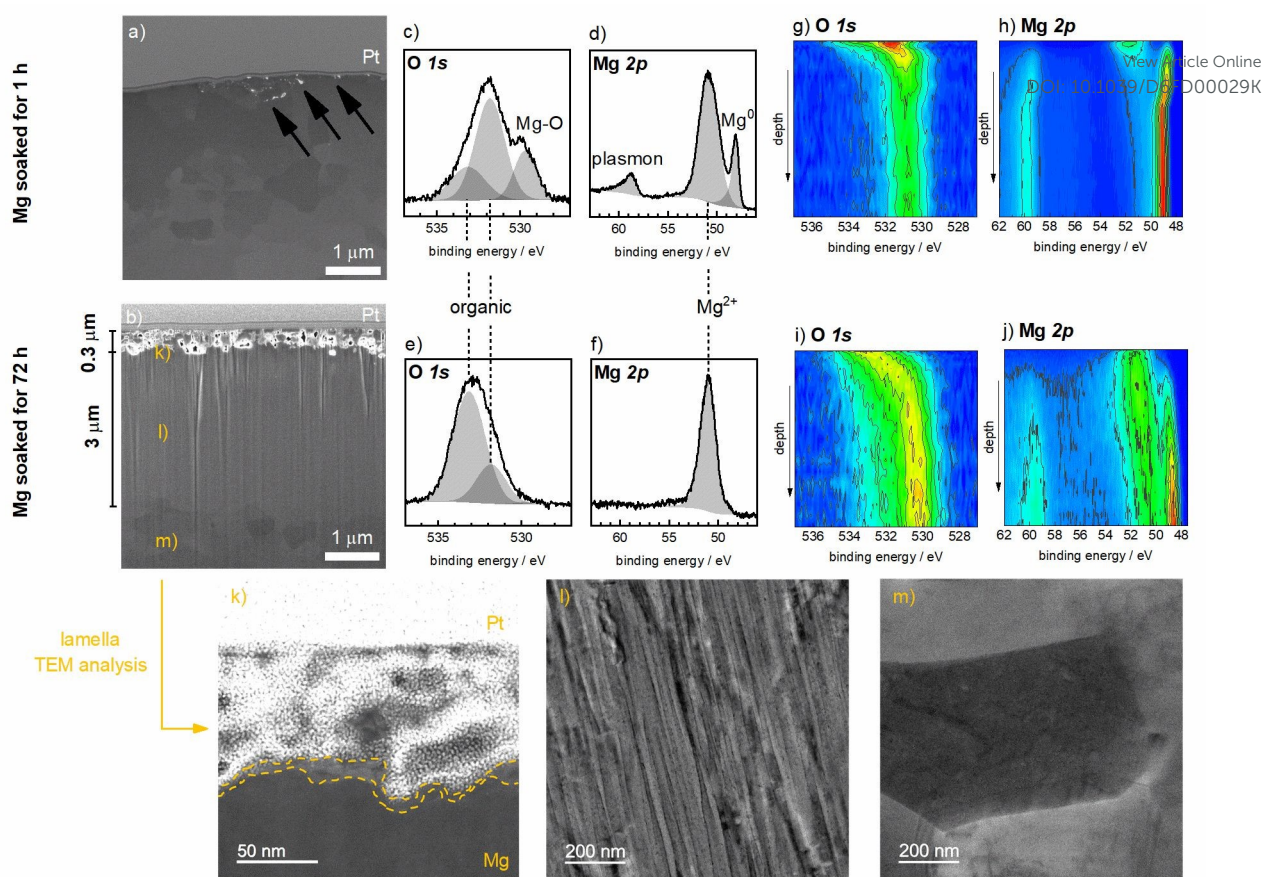


**Figure 3:** Morphological and chemical composition of the passivation layer on Mg metal: a) FIB-SEM cross section of the Mg electrode soaked in the electrolyte for 1 h, b) FIB-SEM cross section of the Mg electrode soaked in the electrolyte for 72 h, c) and d) O 1s and Mg 2p XPS spectra of the Mg electrode surface after 1 h soaking, respectively, e) and f) O 1s and Mg 2p XPS spectra of the Mg electrode surface after 72 h soaking, respectively, g) and h) O 1s and Mg 2p XPS spectra during sputtering of the Mg electrode surface after 1 h soaking, respectively, i) and j) O 1s and Mg 2p XPS spectra during sputtering of the Mg electrode surface after 72 h soaking, respectively k) HAADF-STEM image of the topmost region of the FIB-prepared lamella from the 72 h sample, showing a porous surface layer heavily influenced by Pt deposition, and a denser subsurface layer (yellow dashed line), TEM micrographs of the l) middle region of the lamella, and m) bottom region of the lamella.

The surface of the Mg sample soaked for 1 h shows a few pores at the top of the electrode, (black arrows pointing to white spots, **Fig. 3a**), while an approximately 300 nm thick porous layer is evident on the sample soaked for 72 h (**Fig. 3b**), suggesting a significantly different passive layer thickness. Furthermore, in the 72 h sample, the topmost 3  $\mu\text{m}$  of bulk magnesium shows a changed structure with no visible grain boundaries. The high resolution Mg 2p XPS spectrum of the 1 h soaked sample shows the presence of peaks attributed to elemental  $\text{Mg}^0$  (**Fig. 3d**), while for the 72 h sample no  $\text{Mg}^0$  is evident (**Fig. 3f**), supporting the FIB-SEM analysis and suggesting growth of



1 the passive layer thickness. The O 1s XPS spectrum shows the presence of MgO and  
2 organic oxygen compounds in the 1 h sample (**Fig. 3c**), while in the 72 h sample no  
3 MgO is evident and additional changes in organic oxygen compounds are detected.

4 The samples were further examined through XPS depth profiling, which confirmed that  
5 the layer in the 1 h sample is thinner compared to the 72 h sample (**Figs. 3h and j**).  
6 Namely, the sputtering depth required until Mg<sup>0</sup> is detected (peak at approximately 49  
7 eV and plasmon signal 12 eV higher) is significantly smaller for the 1 h sample than for  
8 the 72 h sample. Note that we have a residual O 1s spectra signal that never decreases  
9 in both samples (**Figs. 3g and i**), the origin of which is unclear. This could be due to  
10 oxygen present in the sample, degradation from the sputtering procedure, or re-  
11 passivation by residual oxidizing compounds in the XPS chamber<sup>13</sup>. The final oxygen  
12 and magnesium peak positions differ between the 1 h and 72 h samples (530.7 eV vs.  
13 530.2 eV and 49.1 eV vs. 48.6 eV), but their binding energies are the same relative to  
14 each other. We propose that the oxygen peak arises from the same chemical species,  
15 while the position differs due to the identical calibration procedure used for samples  
16 with significantly different passive layer thicknesses. Namely, the spectra were  
17 calibrated to adventitious carbon peak, which is a surface species. Since we expect  
18 the passive layer to be a poor electronic conductor, a gradient in the electrostatic  
19 potential with depth is likely affecting the binding energy of the species located at  
20 deeper levels, shifting their binding energy positions.

21 At first glance, this analysis reveals a very pronounced discrepancy between the EIS  
22 data and the FIB-SEM/XPS analysis. The former suggest a passivation layer on the  
23 order of a nanometer, while the FIB-SEM/XPS results indicate much thicker, porous  
24 and heterogeneous structures that differ significantly between the two examined  
25 samples in morphology, thickness and chemical composition. To explain this apparent  
26 mismatch, we propose a model similar to Li metal passivation: a thin, compact  
27 passivation layer directly in contact with the metal and a thicker, porous passivation  
28 layer on top<sup>10</sup>. The two layers differ in their preferential modes of transport. Due to the  
29 open structure of the upper layer, transport occurs through migration and diffusion in  
30 the liquid electrolyte trapped in the pores of the passivation layer. The compact  
31 passivation layer beneath this porous one, however, requires solid-state conduction.  
32 For Li metal, the conductivity of this layer for Li<sup>+</sup> ions is high (i.e., it is an SEI), while  
33 the compact passivation layer on Mg metal does not allow Mg<sup>2+</sup> migration through it  
34 (i.e., it is not an SEI), resulting in significantly larger associated resistances.

35 To further characterize the passivation layer and visualize its thickness, the 72 h  
36 sample was processed using FIB-SEM to produce an electron-transparent lamella,  
37 which was then examined by transmission electron microscopy (TEM/STEM). For  
38 lamella preparation, we intentionally selected a region on the electrode with a thinner  
39 porous surface layer to produce a more stable lamella that would not decompose  
40 during handling or transfer between instruments. Three different points on the lamella  
41 were examined with TEM/STEM, as labeled in **Fig. 3b**. The top part of the lamella  
42 corresponds to the porous surface layer previously observed by FIB-SEM. This region



1 appeared significantly affected by protective Pt deposition applied during FIB-SEM  
2 preparation, as indicated by its increased brightness (with brightness being roughly  
3 proportional to the square of the atomic number) in HAADF-STEM imaging (**Fig. 3k**).  
4 Notably, directly beneath this Pt-affected porous layer, a denser and more uniform  
5 layer with a thickness of approximately 7-10 nm was observed (**Fig. 3k**, yellow dashed  
6 lines). We interpret this feature as the compact passivation layer probed by EIS. The  
7 thickness of this layer and the capacitance obtained from EIS suggest that its dielectric  
8 constant is in the range of 4.8–6.9, a reasonable value for layers of similar composition,  
9 especially when defects are considered (noting that MgO has a permittivity around 10).  
10 The bottom layer showed crystalline Mg with a grain size of approximately 0.5  $\mu\text{m}$  in  
11 diameter (**Fig. 3m**), while the middle layer exhibited a mixture of amorphous and  
12 crystalline Mg (**Fig. 3l**). We attribute this change to the consumption of Mg metal during  
13 surface passivation layer formation.

14 Although we took care to minimize the effects of sample handling during *ex-situ*  
15 analysis, we acknowledge that the procedure might have affected the interfaces we  
16 attempted to characterize. An example of such interference was discussed in the XPS  
17 depth-profiling experiment, where residual oxygen species were present regardless of  
18 sputter time. Although *operando* analysis would improve the validity of the results, it  
19 often requires special setups or even synchrotron use<sup>14,15</sup>. Therefore, our approach is  
20 to emphasize the differences between the two samples (1 h vs. 72 h), which were  
21 handled identically. The most significant differences are the presence of a several  
22 hundred nanometer thick porous layer on the 72 h sample and the absence of inorganic  
23 species on its surface. Combined with the EIS analysis, these differences suggest that  
24 Mg metal forms a dual passivation layer in the examined electrolyte, consisting of a  
25 thin, compact passive layer (up to 10 nm thick) directly on the surface of the bulk Mg  
26 metal, and a porous, open passive layer (up to several hundred nanometers thick,  
27 depending on the electrode's contact time with the electrolyte) on top of the compact  
28 layer. From top to bottom, the passive layer becomes less organic and more inorganic  
29 in nature. In impedance measurements, only the compact layer is detected, as it is  
30 poorly conductive and exhibits high resistance. In contrast, the porous passivation  
31 layer permits mass/charge transport through the electrolyte within its pores, so its  
32 resistance is likely small and insignificant.

33 After examining the electrodes at OCV, the next question is what happens when  
34 current is applied. This was studied using a three-electrode cell with excess electrolyte,  
35 where WE, CE and RE were all Mg foil strips. The reference electrode compartment  
36 was physically separate from the WE and CE compartment, but was connected to it by  
37 an electrolyte bridge with a glass fiber connection. The electrodes were polarized at  
38 different current densities (10, 3, 1, and 0.3  $\text{mA}\cdot\text{cm}^{-2}$ ), with the total capacity kept  
39 constant by varying the time of the experiment. The experiment revealed an asymmetry  
40 in the response between the stripped and plated sides (**Fig. 4a**). Specifically, after a  
41 certain period, the overpotential on the stripped electrode side abruptly drops by more  
42 than a tenfold (from 500 mV to 40 mV, then decreases further). This abrupt drop in



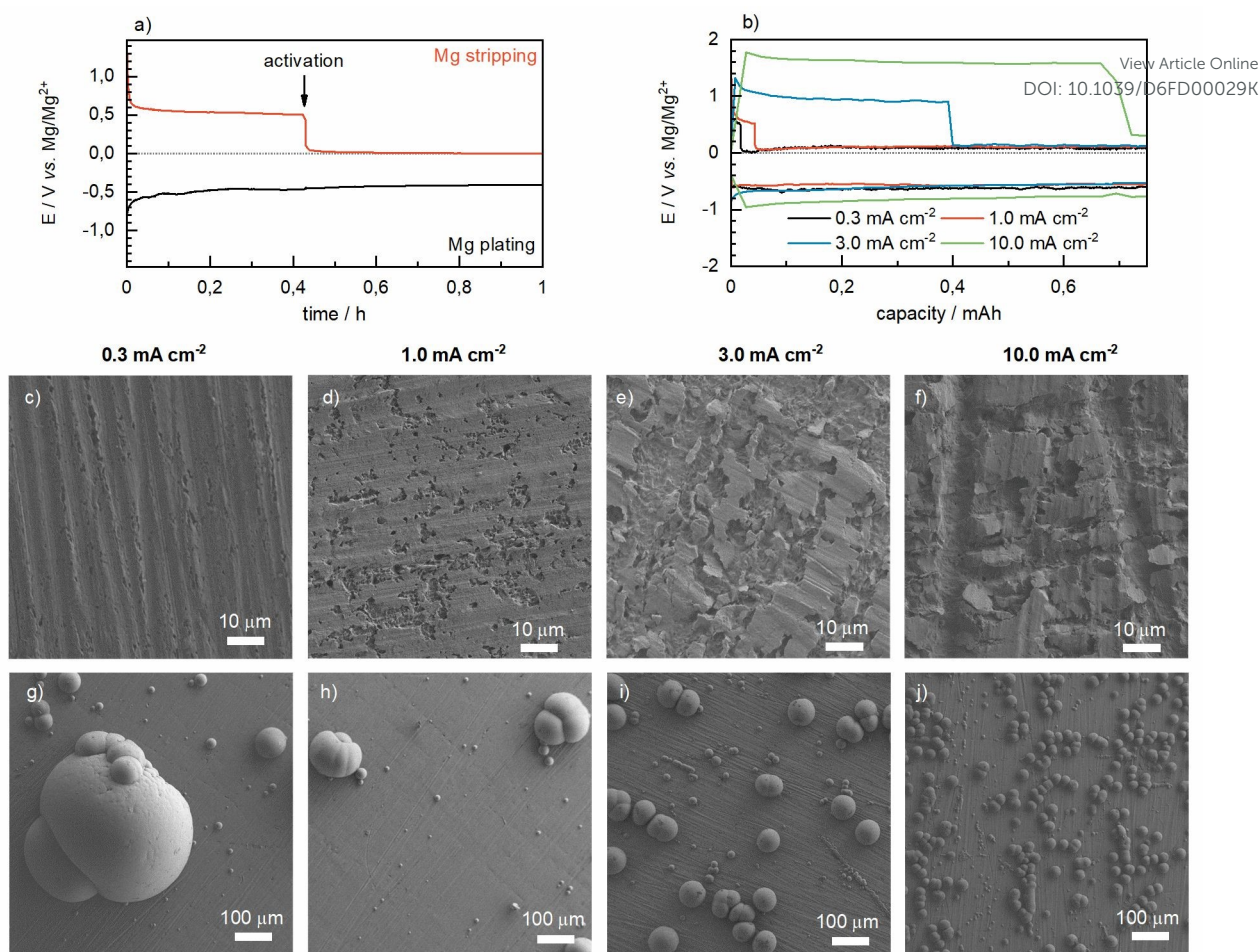
1 overpotential has been observed multiple times during cycling of Mg metal batteries  
2 and is attributed to activation of the electrode through mechanical breakage of the non-  
3 conductive passivation layer.<sup>16–19</sup>

4 If the current density is varied, the time at which this activation occurs remains roughly  
5 constant (between 0.5 and 1.5 h). This means that more charge passes at higher  
6 current densities before the electrode is activated (i.e., the drop in overpotential in **Fig.**  
7 **4b** occurs at higher capacities for higher currents). The overpotential before activation  
8 does not show a clear correlation with the applied current. It is generally higher for  
9 larger currents, but does not scale directly with the difference. After activation, when  
10 the overpotentials are significantly lower, variation with current is more pronounced:  
11  $94 \pm 6$  mV,  $84 \pm 30$  mV,  $150 \pm 30$  mV, and  $310 \pm 10$  mV for 0.3, 1.0, 3.0, and  
12  $10.0 \text{ mA}\cdot\text{cm}^{-2}$ , respectively (measured in at least three repetitions for each current).  
13 Nevertheless, we are not comfortable drawing direct conclusions from these values,  
14 since the reference electrode used was Mg metal, which we do not consider stable or  
15 reliable enough to detect differences on the order of 10 mV between different cells.

16 SEM analysis of the electrodes shows an increasing percentage of the surface covered  
17 with pits with as the current increases (**Figs. 4c-f**). Since the amount of Mg removed  
18 from the electrode was kept constant in all experiments, this suggests the presence of  
19 a porous network of missing Mg beneath the apparent surface, with few pits in the  
20 topmost layer (**Fig. 4c**). SEM micrographs of the plated electrode at the tested current  
21 densities show a decrease in the size of the deposits and an increase in the density of  
22 the coverage as the current increases (**Figs. 4g-j**), an effect well known from the  
23 theory of electrodeposition.

24 Interestingly, none of the plated electrode surfaces show any breakage in the  
25 passivation layer, with lines from mechanical brushing during electrode preparation still  
26 visible. This aligns with the observation that the plated electrode does not exhibit the  
27 same activation behavior as the stripped electrode (**Fig. 4a**). Additionally, the  
28 overpotentials at different currents show minimal variation during plating, with 0.3, 1.0,  
29 and  $3.0 \text{ mA}\cdot\text{cm}^{-2}$  current densities all resulting in approximately 550 mV overpotential.  
30 At  $10 \text{ mA}\cdot\text{cm}^{-2}$ , a larger difference (800 mV, **Fig. 4b**) is observed, but this is still far  
31 less than the several-fold difference that would mimic the current change.





1  
2 **Figure 4:** a) overpotentials during stripping and plating b) at various current densities  
3 and SEM micrographs for the stripped electrode (c-f) and plated electrode (g-j) at the  
4 tested current densities.

5  
6 This raises the question of the underlying mechanism of deposition. Since  
7 electrochemical experiments provide no evidence of electrode activation and SEM  
8 analysis indicates an intact passivation layer at the examined size scale, we suggest  
9 that Mg deposition may occur while maintaining the passivation layer intact. We  
10 hypothesize that this is possible through relatively fast electronic transport through the  
11 passivation layer, particularly under voltage bias. Such transport can occur via electron  
12 tunneling, which is significantly enhanced under voltage bias (following a cubic law),  
13 as known from the literature (Simmons model)<sup>20</sup>. Thus, for Mg deposition to occur, the  
14 electron can tunnel from the metal side through the passivation layer and react with  
15  $Mg^{2+}$  ions in the electrolyte, resulting in the deposition of a new metal layer on top of  
16 the passive film. This mechanism is straightforward, preserving the original state of the  
17 passivation layer and eliminating the need for electrode activation. In contrast, the  
18 mechanism during stripping must be very different, as this process requires  $Mg^{2+}$  ions  
19 to form below the passive film and then pass through the region occupied by the  
20 passive film. Since the film is ionically non-conductive, this passage can only occur if



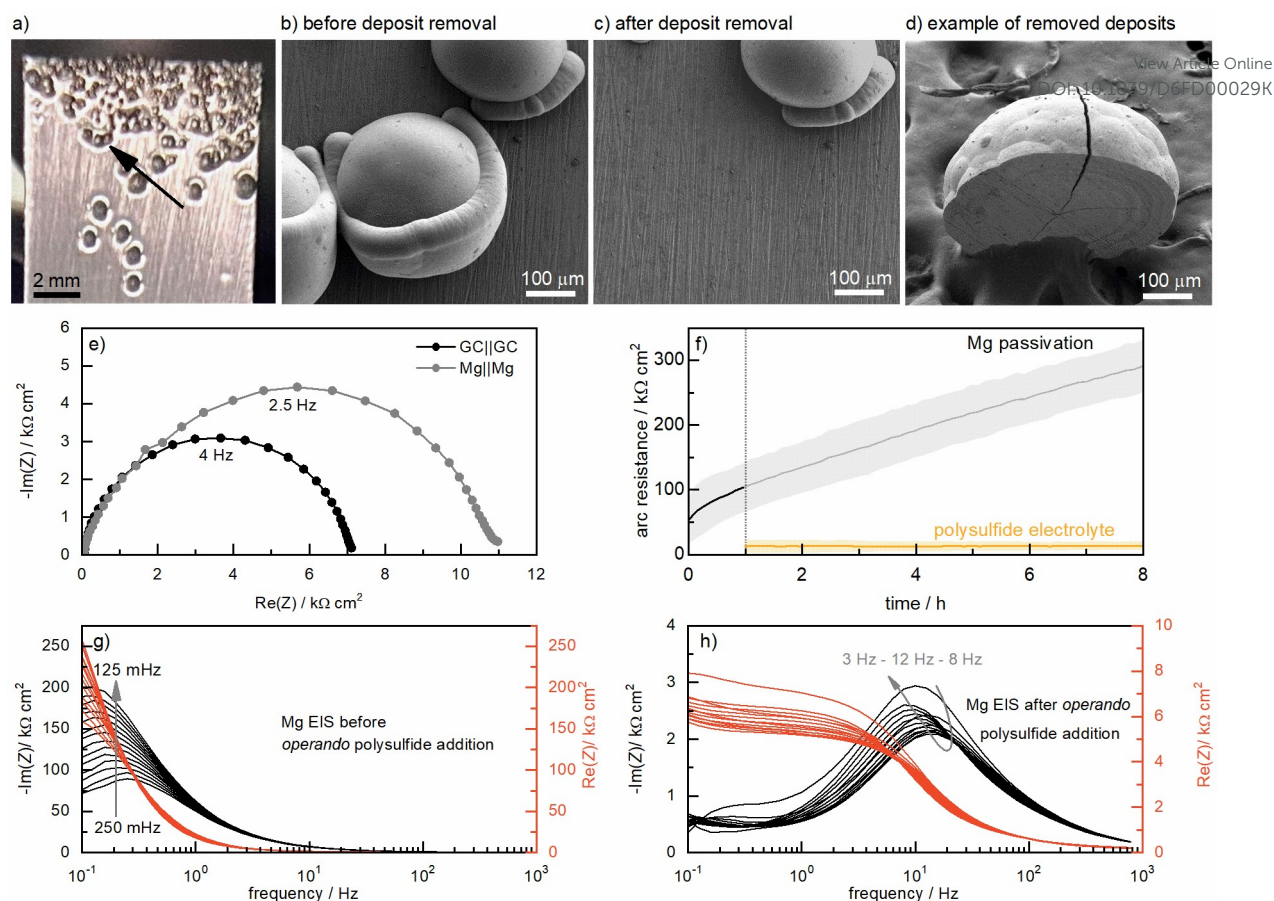
1 the passivation layer breaks, which is usually observed in galvanostatic experiments  
2 as the activation of the electrode immediately (soon) after imposing a galvanostatic  
3 step to the OCV conditions.

4 One aim of this contribution was to support the hypothesis that the passivation layer  
5 on Mg is electronically conductive. To address this, we conducted two different  
6 experiments: one electrochemical and one morphological. Since we assume that  
7 deposits form on top of the passivation layer created under OCV conditions, this  
8 implies that (i) the deposits are relatively weakly bound to the electrode surface and  
9 (ii) there is no “stem” connecting the deposit to the bulk Mg. To test this, we used an  
10 electrode onto which Mg was deposited in relatively large, visually observable  
11 deposits, spaced far enough apart to allow selective mechanical removal of some  
12 deposits (**Fig. 5a**; the arrow indicates the removed deposit). The electrode was  
13 examined by SEM before being returned to the glovebox, where some deposits were  
14 carefully scraped off without damaging the electrode surface. The sample was then  
15 washed again to remove any electrolyte salt trapped underneath, in order to check  
16 whether a “stem” was present.

17 As shown in the SEM micrograph of the deposit before removal, the electrode surface  
18 displayed a morphology similar to that observed in the previous experiment where the  
19 current density was varied (**Figs. 4g-j**). The area around the deposit was smooth and  
20 free of cracks, with visible indentations caused by brushing the Mg surface with  
21 sandpaper during electrode preparation. The selected deposit was round, with a total  
22 diameter of 0.5 mm, and consisted of several merged grains (**Fig. 5b**). After the deposit  
23 was removed, the electrode surface underneath showed no evidence of a connection  
24 between the bulk electrode and the removed deposit, nor any breakage in the  
25 passivation layer (**Fig. 5c**). We also found some of the removed deposits produced  
26 during sample handling on the surrounding carbon tape on the SEM stage.  
27 Micrographs of their bottom surfaces mirrored the Mg brushing marks and further  
28 support the hypothesis that Mg is deposited on top of a stable passivation layer (**Fig.**  
29 **5d**). We assume cracking of the deposit happened due to either washing or physical  
30 removal of the deposits.

31





1  
 2 **Figure 5:** Identical location microscopy on a sample of a magnesium metal electrode  
 3 with large electrochemical deposits. a) shows a photograph of the sample with the  
 4 arrow pointing to the deposit examined with the microscope, SEM micrographs b)  
 5 before, c) after deposit removal, and of d) example of removed deposits. e) EIS spectra  
 6 of 100 mM  $\text{Li}_2\text{S}_8$  in TEGDME:DOL 1:1 (v:v) solution in symmetrical GC||GC or Mg||Mg  
 7 cell, f) comparison of the high frequency arc resistance growth in Mg||Mg cell during  
 8 passivation at OCV with a  $\text{Mg}^{2+}$  electrolyte (black/grey line with the shaded area  
 9 showing standard deviation) and in a Mg||Mg cell after 1 h vial passivation and  
 10 subsequent cell assembly with 100 mM  $\text{Li}_2\text{S}_8$  in TEGDME:DOL 1:1 (v:v) (yellow line  
 11 with the shaded area showing standard deviation), g) bode plots of impedance spectra  
 12 of Mg electrode before operando polysulfide addition (1 h of passivation) and f) Bode  
 13 plots of impedance spectra of Mg electrode after operando polysulfide addition (1 h of  
 14 stabilization).

15  
 16 Additionally, we attempted to demonstrate that the passivation layer exhibits electronic  
 17 conductivity by measuring the electrochemical impedance response of a symmetrical  
 18 Mg||Mg cell with a polysulfide-containing electrolyte. Lithium polysulfides have been  
 19 extensively studied as intermediate electroactive compounds in Li-S batteries. They  
 20 readily dissolve in several ether-based electrolytes, with the catholyte typically  
 21 containing various polysulfide oxidation states due to their tendency to disproportionate  
 22 and coproportionate. When polysulfide species are added to a planar glassy carbon



1 symmetrical cell, their impedance response usually displays a large (several  $\text{k}\Omega\cdot\text{cm}^2$ )  
2 arc due to the charge transfer reaction of the polysulfide species on the glassy carbon  
3 surface. The characteristic peak frequency of this arc is in the range of 1–20 Hz (**Fig.**  
4 **5e**, black spectrum).

5 The Mg symmetrical cell was assembled using Mg electrodes that were pre-passivated  
6 for 1 hour by soaking the electrode discs in a vial containing the Mg electrolyte. The  
7 electrodes were washed with dioxolane solvent before being used for cell assembly  
8 with a polysulfide-containing electrolyte without Mg salt. If the passivated electrodes  
9 exhibited neither ionic nor electronic conductivity, the resulting impedance spectrum  
10 with polysulfide addition would be blocking in nature and would not display any of the  
11 previously described characteristics. However, the measured impedance spectrum  
12 matched the expected response of a single arc of several  $\text{k}\Omega\cdot\text{cm}^2$  at 1–20 Hz (**Fig. 5e**,  
13 grey spectrum). Additionally, the evolution of the impedance spectra was monitored for  
14 several hours. The polysulfide-containing Mg||Mg cell showed very stable impedance  
15 spectra with minimal variation (**Fig. 5f**, yellow lines), in stark contrast to the significant  
16 impedance growth previously discussed for a symmetrical Mg cell at OCV (**Fig. 5f**,  
17 grey lines).

18 We additionally repeated this experiment using an *operando* setup. Instead of pre-  
19 passivating the Mg electrodes, washing them and then using polysulfide containing  
20 electrolyte for cell assembly, we conducted the experiment without any disturbance to  
21 the interfaces. For this experiment, the cell shown in **Figs. 1c and 1d** was used in a  
22 two-electrode configuration. The evolution of the impedance spectra was monitored for  
23 one hour at open circuit voltage to allow the electrodes to passivate. During this time,  
24 the resistance of the measured arc increased from approximately  $180\text{ k}\Omega\cdot\text{cm}^2$  (250  
25 mHz) to  $400\text{ k}\Omega\cdot\text{cm}^2$  (125 mHz), see **Fig. 5g**. After one hour, 0.5 M  $\text{Li}_2\text{S}_8$  solution was  
26 added to the cell, diluting the polysulfide solution to 0.1 M. Upon this *operando*  
27 polysulfide addition, the impedance response changed drastically, decreasing to  
28 approximately  $2.5\text{ k}\Omega\cdot\text{cm}^2$  with a peak frequency between 3 Hz and 12 Hz. **Figs. 5h**  
29 show the measured data for 1 h after polysulfide addition. Apart from the significant  
30 100-fold decrease in impedance, the spectra also showed much better stability.  
31 Overall, the *operando* experiment supports the previously conducted tests and the  
32 hypothesis of significant electronic conductivity of the Mg surface passivation layer.

### 33 **Discussion of the effect of interphase properties on Mg anode operation**

34 With this new knowledge, we need to revisit all previous experiments and discuss how  
35 the electronic conductivity of the passive layer affects the explanations of the observed  
36 phenomena. The behavior of the Mg electrode was shown to differ significantly from  
37 that of the lithium metal anode. We attribute this primarily to the inherently poor  
38 conductivity of Mg ions in solids, as exemplified by the scarcity of solid-state Mg-ion  
39 conductors. Consequently, we exclude the possibility that the Mg passivation layer  
40 functions as a Solid Electrolyte Interphase (SEI). By definition, an SEI is characterized  
41 by high ionic conductivity and negligible electronic conductivity. In contrast, the passive



1 film observed on Mg exhibits poor ionic conductivity and significant electronic  
2 conductivity. Electrochemical impedance spectroscopy and morphological analysis  
3 were used to quantify these transport parameters, as shown below. Faraday Discussions Online  
DOI: 10.1039/D6FD00029K

4 Continuous surface passivation under OCV conditions and the formation of a porous  
5 passivation layer can occur only when both electrons and Mg ions cross the  
6 passivation layer. The measured thickness of the porous passivation layer (**Fig. 3b**)  
7 allows estimation of the capacity associated with this corrosion process. This capacity  
8 is directly related to the resistance from Mg ion migration in the compact passivation  
9 film, as this migration is more difficult than electron tunneling in the studied system and  
10 thus determines the overall corrosion rate. Assuming 50% porosity and a 300 nm  
11 thickness of MgO formed over 72 hours of reaction time yields a current of 0.8  $\mu\text{A}$ . With  
12 an estimated voltage difference of 1 V, the resistance for Mg ion migration through the  
13 compact passivation film is in the  $\text{M}\Omega\cdot\text{cm}^2$  range.

14 To measure the electronic resistance of the layer, the polysulfide experiments  
15 described above can be used. In these experiments, the resistance difference between  
16 the GC||GC cell and the Mg||Mg cell was 4  $\text{k}\Omega\cdot\text{cm}^2$  (**Fig. 5e**). This value can be  
17 attributed to the electronic resistance of the layer. However, it is important to consider  
18 that (i) polysulfides disproportionate, which can shift the resistance of the arc back and  
19 forth<sup>17</sup>, and (ii) the ionic conductivity of the layer is not infinitely large, so some  
20 corrosion occurs, reducing polysulfides and increasing the arc resistance in Mg||Mg  
21 cells. Therefore, the conclusion is that the resistance for electron tunneling through the  
22 layer at open-circuit voltage is at most a few  $\text{k}\Omega\cdot\text{cm}^2$ . Notably, according to the  
23 Simmons model<sup>16</sup>, this value decreases according to a cubic law when the cell is under  
24 bias, so the resistance due to electron passage during galvanostatic measurements is  
25 considerably lower.

26 Using these parameter values, we first examine the OCV response of the Mg metal  
27 anode. As shown in **Fig. 2**, the resistance values during the first 20 hours of  
28 measurement increase from 40 to 400  $\text{k}\Omega\cdot\text{cm}^2$ , while the capacitance remains  
29 relatively stable at approximately 17  $\mu\text{F}\cdot\text{cm}^{-2}$ . As hypothesized, the resistance drift  
30 could result from a decrease in passive layer conductivity, changes in active reaction  
31 sites, or both. We assume that at OCV, the ionic and electronic resistances are in  
32 parallel (since either can contribute to the electrochemical response) and are followed  
33 in series by the charge transfer reaction coupled with double-layer capacitance.  
34 Because the passive layer resistances are in parallel, the resulting resistance will be  
35 less than the smaller electronic resistance. Therefore, the OCV EIS spectra are  
36 expected to show a contribution from passive layer resistance of less than a few  
37  $\text{k}\Omega\cdot\text{cm}^2$ .

38 Since this calculated value is much smaller than the measured impedance (**Fig. 2**), it  
39 is most likely that, among the three possible explanations for the phenomenon, only  
40 the charge transfer reaction is being observed. We believe the measured impedance  
41 increase results from changes in the availability of suitable reaction sites on the passive



1 layer surface, which are affected by passive layer reordering. We propose that the  
2 effect of changes in suitable reaction sites is correlated with the multi-step nature of  
3 Mg reactions, which include surface-adsorbed species, as this adsorption process can  
4 be highly specific to the exact surface chemistry.<sup>18</sup>

5 Let us now consider the data collected when the cell is under bias. As discussed, the  
6 asymmetry of the processes, poor ionic conductivity, and good electronic conductivity  
7 suggest that stripping occurs through the breakage of the passive layer, exposure of  
8 bare Mg, and reactions at those open sites. This implies that (i) the impedance  
9 measured on the electrode during stripping after activation reflects the charge transfer  
10 reaction on an (as yet unknown) percentage of the Mg electrode, where bare Mg was  
11 exposed during activation, and (ii) before activation, we should observe very large  
12 overpotentials ( $1 \text{ M}\Omega \cdot \text{cm}^2$  times the current density). In our experiments, this would  
13 result in 300 V to 1 kV of overpotential, depending on the applied current. However,  
14 this value is never actually observed in measurements, not even in cases where we  
15 initially assumed the electrode was non-activated (before “activation” in galvanostatic  
16 experiments, **Fig. 4a**). With this additional knowledge, we presume that the largest  
17 activation occurs at very short times upon applying a current bias, when we do not  
18 detect it with the employed measurement settings. The second drop is likely an  
19 additional, second-step activation process. At this point, we do not have a solid  
20 explanation for why the second activation occurs and why the time at which it occurs  
21 is nearly constant.

22  
23 For the electrode undergoing stripping, we assume that the activated surface area  
24 directly correlates with the current responsible for activation, while the measured  
25 charge transfer reaction resistance is directly associated with the size of the open  
26 surface area. Thus, higher currents activate more of the electrode and more  
27 significantly reduce the charge transfer resistance. This effect explains why we do not  
28 observe a clear correlation between current density and overpotential values. Since  
29 the exact degree of surface activation is unknown, it is also difficult to reconstruct the  
30 voltage-current characteristic, so we do not know the specific effect that current density  
31 has on the charge transfer reaction resistance. Nevertheless, we know that the total  
32 charge transfer reaction resistance contributions for Mg oxidation are relatively small,  
33 since the total resistance values calculated from the current and overpotential after the  
34 second activation step vary between approximately 30 and  $300 \text{ }\Omega \cdot \text{cm}^2$  (for  $10 \text{ mA} \cdot \text{cm}^{-2}$   
35 and  $0.3 \text{ mA} \cdot \text{cm}^{-2}$ , respectively; assuming the Mg reference electrode is stable).

36 On the plated side, the situation is fundamentally different. Due to the electronic  
37 conductivity of the passive layer, we assume that after initial deposition at isolated  
38 preferential reaction sites (where the reaction occurs during OCV), the plating reaction  
39 rapidly spreads over most of the electrode surface. The already deposited atoms serve  
40 as low-energy anchors for further metal deposition. Unlike stripping, which after  
41 activation is largely determined by the reaction mechanism, the rate of plating depends



1 on both electron conduction through the passive layer and the deposition reaction  
2 itself. Thus, the corresponding impedance response consists of arcs representing the  
3 electronic resistance of the passive layer and the charge transfer reaction. Both  
4 decrease when current bias is applied – the former drops with the cube of the current  
5 according to the Simmons model, while the latter decreases according to the voltage-  
6 current characteristic, which depends on the actual mechanism, currently unknown.  
7 However, some predictions about the current-overvoltage characteristic can still be  
8 made based on the general behavior of multistep electrochemical reactions involving  
9 multivalent ions, as discussed below. A further complication in this system is that the  
10 response is inherently connected to changes in morphology, which, as shown, is  
11 directly affected by the current density (**Figs. 4g–j**). Nevertheless, we estimated the  
12 surface difference between the lower and higher currents used and found minimal  
13 differences in size.

14 Our data for the specific electrolyte and currents tested show that the overpotentials  
15 remain constant at lower currents and are slightly higher at the highest current tested.  
16 We assume this difference may result from the formation of concentration gradients  
17 and mass transport limitations at  $10 \text{ mA}\cdot\text{cm}^{-2}$ . Because the electrode's total surface  
18 area is minimally affected by the morphologically different deposits and there is no  
19 clear variation in overpotential during the experiment when deposits are made, we  
20 reject the hypothesis that the overpotential variation (or lack thereof) is geometrical in  
21 origin. Furthermore, if electronic resistance was the main bottleneck, we would expect  
22 a clear change in overpotentials with changes in current density – a tenfold increase  
23 in current should correspond to a thousandfold increase in resistance.

24 We therefore believe it is more likely that the charge transfer reaction contribution  
25 controls the operation. The minimal overpotential variation between  $0.3 \text{ mA}\cdot\text{cm}^{-2}$  and  
26  $3 \text{ mA}\cdot\text{cm}^{-2}$  (Fig. 3b) can be explained by a current-voltage curve with very little change  
27 in current up to a certain overpotential, followed by activation of the reaction  
28 (approximated by an exponential relationship) at higher overvoltages, which is  
29 characteristic of multistep reactions (see examples in references<sup>18,19</sup>). This also  
30 suggests a significantly different order of magnitude for charge transfer resistance  
31 between stripping and plating, which, apart from the inherent asymmetry of oxidation  
32 versus reduction, is assumed to be affected by the fact that one occurs on bare Mg,  
33 while the other takes place on top of the passive film.

34 The impedance of both oxidized and reduced Mg electrodes is therefore controlled by  
35 charge transfer reactions, but there is an inherent difference in where these reactions  
36 occur. During stripping, the ionically non-conductive passive layer must break to  
37 expose bare Mg. Not all of the electrode is active, yet we typically observe low  
38 associated resistances. In contrast, the mechanism differs due to the electronic  
39 conductivity of the interphase, as deposition can occur on top of the passive layer. In  
40 this case, the entire surface area of the electrode is inherently active, but the  
41 resistances are significantly larger (approximately tenfold, as estimated from  
42 overpotentials while disregarding the non-linearity of the current-voltage curve). We



1 assume this may be because the reduction reaction occurs on the passive film, while  
2 oxidation occurs on bare Mg.

View Article Online  
DOI: 10.1039/D6FD00029K

### 3 **Conclusions**

4 This work elucidates the complex structure and transport properties of the interphase  
5 formed on magnesium metal in chloride-based electrolytes. Contrary to the classical  
6 Solid Electrolyte Interphase (SEI) model observed in lithium batteries—which relies on  
7 high ionic conductivity and electronic insulation—our findings show that the interphase  
8 between magnesium and electrolyte behaves as a relatively good electronic conductor  
9 and very poor conductor for magnesium ions.

10 We identified a dual-layer structure comprising of a thin (~7–10 nm) compact inner film  
11 and a thicker (up to several hundred nanometers) porous outer layer that facilitates  
12 liquid-phase transport of Mg<sup>2+</sup> ions. This unique architecture creates a fundamental  
13 asymmetry in the anode's operation. During stripping, the ionically insulating nature of  
14 the compact layer forces the physical rupture of the film to expose bare magnesium.  
15 Conversely, plating does not require film breakage; instead, the electronic conductivity  
16 of the passivation layer allows magnesium reduction to occur on top of the interphase,  
17 likely facilitated by electron tunneling. These results indicate that the performance of  
18 magnesium anodes is governed by charge transfer reactions that are largely dictated  
19 by the specific properties of this passive film. Additionally, it is important to recognize  
20 that reaction losses are closely linked to the properties of the interphase. On the  
21 stripped side, electrode performance is limited by the degree of electrode activation,  
22 while on the plated side, it is determined by the specific reactivity of the surface sites  
23 where the charge transfer reaction occurs. The finding that the interphase is  
24 electronically conductive challenges the applicability of traditional SEI engineering  
25 strategies for magnesium batteries. Rather than solely focusing on ionic transport,  
26 future electrolyte and interface designs must account for the electronic leakage across  
27 the passivation layer and the dynamics of film rupture and repair.

### 29 **CRedit author statement**

30 SDT: conceptualization, data curation, formal analysis, funding acquisition,  
31 investigation, methodology, supervision, validation, visualization, writing – original  
32 draft; JM: conceptualization, methodology; BS: investigation; ČS: investigation; OL:  
33 investigation; TŠ: investigation; ET: investigation; ID: investigation; NL: investigation,  
34 formal analysis; UK: investigation, formal analysis; GK: investigation, formal analysis;  
35 MG: conceptualization, formal analysis, supervision, writing – original draft; RD:  
36 funding acquisition, writing – review & editing.

37

### 38 **Conflicts of interest**

39 There are no conflicts of interest to declare.



1

## 2 Acknowledgements

3 The authors acknowledge the funding from the Slovenian Research Agency ARIS  
4 (core program funding P2-0423). SDT acknowledges financial support by the Slovene  
5 Research Agency ARIS with research project Z2-4465 funding. The research was  
6 cofunded under the HyBReED project, supported by the European Union -  
7 NextGenerationEU.

8

## 9 Data availability

10 Data for this article are available at Zenodo repository at  
11 <https://doi.org/10.5281/zenodo.18746519>.

12

## 13 References

- 14 1. J. Long, Y. Liu, Z. He, S. Tan, F. Xiong, H. Xu, W. Wang, G. Zhang, Z. Yang, and  
15 Q. An, *ACS Nano*, **18**, 15239–15248 (2024).
- 16 2. D. Zhang, Y. Wang, Y. Yang, Y. Zhang, Y. Zhao, M. Pan, Y. Sun, S. Chen, X. Liu,  
17 J. Wang, and Y. NuLi, *Adv. Energy Mater.*, **13** (2023).
- 18 3. M. Chen, S. Zhang, X. Ge, Z. Yang, G. Sun, A. Du, J. Zhao, S. Li, J. Xiao, H. Li,  
19 and G. Cui, *Advanced Materials*, **37** (2025).
- 20 4. Z. Fan, W. Zhao, S. Shi, M. Zhou, J. Li, Y. Liu, Z. Pan, and X. Yang, *Angew.*  
21 *Chem. Int. Ed.*, **64** (2025).
- 22 5. X. Chai, H. Xie, T.-T. Zhang, Y. Xin, F. Zhang, B. He, H. Xie, L. Yu, and H. Tian,  
23 *Energy Storage Mater.*, **70**, 103460 (2024).
- 24 6. R. Zhang, C. Cui, R. Li, Y. Li, C. Du, Y. Gao, H. Huo, Y. Ma, P. Zuo, and G. Yin,  
25 *Chemical Engineering Journal*, **426**, 130751 (2021).
- 26 7. G. Li, K. Chen, M. Lei, T. Wang, M. Hu, and C. Li, *Adv. Energy Mater.*, **14** (2024).
- 27 8. J. Häcker, T. Rommel, P. Lange, F. Kampmann, J. Remmlinger, Z. Zhao-Karger,  
28 K. A. Friedrich, and M. Nojabae, *Journal of Magnesium and Alloys*, **13**, 2680–2698  
29 (2025).
- 30 9. R. Attias, B. Dlugatch, M. S. Chae, Y. Goffer, and D. Aurbach, *Electrochem.*  
31 *commun.*, **124**, 106952 (2021).
- 32 10. S. Drvarič Talian, J. Bobnar, A. R. Sinigoj, I. Humar, and M. Gaberšček, *The*  
33 *Journal of Physical Chemistry C*, **123**, 27997–28007 (2019).



- 1 11. S. D. Talian, N. Urbanija, and M. Gaberšček, *Solid State Ion.*, **429**, 116987  
2 (2025). View Article Online  
DOI: 10.1039/D6FD00029K
- 3 12. S. Drvarič Talian, G. Kapun, J. Moškon, R. Dominko, and M. Gaberšček, *Nat.*  
4 *Commun.*, **16**, 2030 (2025).
- 5 13. S.-K. Otto, Y. Moryson, T. Krauskopf, K. Pepler, J. Sann, J. Janek, and A.  
6 Henss, *Chemistry of Materials*, **33**, 859–867 (2021).
- 7 14. A. Križan, T. Ericson, L. King, Q. Liu, R. Temperton, R. Dominko, O. Vodeb, D.  
8 Strmčnik, M. Gaberšček, and M. Hahlin, *Physical Chemistry Chemical Physics*, **27**,  
9 7456–7466 (2025).
- 10 15. L. Zhao, M. Feng, C. Wu, L. Guo, Z. Chen, S. Risal, Q. Ai, J. Lou, Z. Fan, Y. Qi,  
11 and Y. Yao, *Nat. Commun.*, **16**, 4283 (2025).
- 12 16. A. Robba, A. Vizintin, J. Bitenc, G. Mali, I. Arčon, M. Kavčič, M. Žitnik, K. Bučar,  
13 G. Aquilanti, C. Martineau-Corcos, A. Randon-Vitanova, and R. Dominko, *Chemistry*  
14 *of Materials*, **29** (2017).
- 15 17. M. V. Bracamonte, A. Vizintin, G. Kapun, F. Cometto, J. Bitenc, A. Randon-  
16 Vitanova, M. Gaberšček, and R. Dominko, *J. Power Sources*, **555**, 232367 (2023).
- 17 18. T. Pavčnik, J. Šuster, E. Tchernychova, J. Bitenc, and R. Dominko, *Batter.*  
18 *Supercaps*, **9** (2026).
- 19 19. A. Vizintin, J. Bitenc, A. Kopač Lautar, K. Pirnat, J. Grdadolnik, J. Stare, A.  
20 Randon-Vitanova, and R. Dominko, *Nat. Commun.*, **9**, 661 (2018).
- 21 20. J. G. Simmons, *J. Appl. Phys.*, **34**, 1793–1803 (1963).
- 22
- 23



## Data availability

Data for this article are available at Zenodo repository at <https://doi.org/10.5281/zenodo.18746519>.

View Article Online  
DOI: 10.1039/C9FD00029K

